The Astronomical Journal, 127:3089–3101, 2004 June

WEAK LENSING FROM SPACE. II. DARK MATTER MAPPING

Richard Massey,[1,2] Jason Rhodes,[2,3,4] Alexandre Refregier,[1,2,5] Justin Albert,[2] David Bacon,[6] Gary Bernstein,[7] Richard Ellis,[2] Bhuvnesh Jain,[7] Tim McKay,[8] Saul Perlmutter,[9] and Andy Taylor[6]

Received 2003 May 27; accepted 2004 March 3

ABSTRACT

We study the accuracy with which weak-lensing measurements could be made from a future space-based survey, predicting the subsequent precision of three-dimensional dark matter maps, projected two-dimensional dark matter maps, and mass-selected cluster catalogs. As a baseline, we use the instrumental specifications of the *SuperNova/Acceleration Probe* (*SNAP*) satellite. We first compute its sensitivity to weak lensing shear as a function of survey depth. Our predictions are based on detailed image simulations created using "shapelets," a complete and orthogonal parameterization of galaxy morphologies. We incorporate a realistic redshift distribution of source galaxies and calculate the average precision of photometric redshift recovery using the *SNAP* filter set to be $\Delta z = 0.034$. The high density of background galaxies resolved in a wide space-based survey allows projected dark matter maps with an rms sensitivity of 3% shear in 1 arcmin^2 cells. This will be further improved using a proposed deep space-based survey, which will be able to detect isolated clusters using a three-dimensional lensing inversion technique with a 1 σ mass sensitivity of approximately $10^{13}\ M_\odot$ at $z = 0.25$. Weak-lensing measurements from space will thus be able to capture non-Gaussian features arising from gravitational instability and map out dark matter in the universe with unprecedented resolution.

Key words: dark matter — gravitational lensing — large-scale structure of universe — space vehicles: general

1. INTRODUCTION

Weak gravitational lensing has now been established as a powerful technique to directly measure the large-scale mass distribution in the universe (for reviews, see Mellier 1999; Bartelmann & Schneider 2001; Refregier 2003b). Several groups have measured the coherent distortion of background galaxy shapes around known galaxy clusters (e.g., Joffre et al. 2000; Dahle et al. 2002) and also statistically in the field (e.g., van Waerbeke et al. 2001; Hoekstra et al. 2002c; Bacon et al. 2003; Jarvis et al. 2003). Ever-growing surveys using ground-based telescopes are beginning to yield useful constraints on cosmological parameters (Hoekstra, Yee, & Gladders 2002b; van Waerbeke et al. 2002; Bacon et al. 2003; Brown et al. 2003). The first two clusters selected purely by weak-lensing mass have now been found and spectroscopically confirmed by Wittman et al. (2001, 2003).

Weak lensing is of such great interest for cosmology because it is directly sensitive to mass. Other observations have traditionally been limited to measuring the distribution of light and linked to theory via complications such as the mass-temperature relation for X-ray–selected clusters (Pierpaoli, Scott, & White 2001; Viana, Nichol, & Liddle 2002; Huterer & White 2002) or the ubiquitous problem of bias (Weinberg et al. 2004). Weak-lensing measurements first avoid these problems, and then have even been used to calibrate other techniques (Huterer & White 2002; Gray et al. 2002; Hoekstra et al. 2002b; Smith et al. 2003). The high resolution, galaxy number density, and stable image quality available from space-based weak-lensing data will allow maps of the projected distribution of dark matter to be reconstructed at unprecedented resolution. The mass power spectrum can be sliced into multiple redshift bins using photometric redshifts, providing a long lever arm for constraints on the evolution of cosmological parameters. Even three-dimensional mass maps, marginally feasible from the ground (Bacon & Taylor 2003), are likely to be sensitive to overdensities as small as galaxy groups from space.

Mass-selected cluster catalogs can also be extracted from such maps (Weinberg & Kamionkowski 2002; Hoekstra 2003). Cluster counts, and the quantitative study of high-sigma density perturbations or higher order shear correlation functions (Bernardeau, van Waerbeke, & Mellier 1997; Cooray, Hu, & Miralda-Escudé 2000; Munshi & Jain 2001; Schneider & Lombardi 2003) are one of the most promising routes to breaking degeneracies in the estimation of cosmological parameters including Ω_m and w, the dark energy equation-of-state parameter. Furthermore, studying well-resolved groups and clusters individually, rather than statistically, will lead to a better understanding of astrophysical phenomena, the nature of dark matter, and the growth of structure under the gravitational instability paradigm (see, e.g., Dahle et al. 2003).

In this paper, we predict the general sensitivity to weak lensing of a space-based wide-field imaging telescope, taking as a baseline the specifications of the proposed *SuperNova/Acceleration Probe* (*SNAP*) satellite. Instrument characteristics, including the point-spread function (PSF), ellipticity patterns, and image stability have been studied in Rhodes et al. (2004, hereafter Paper I). In § 2, we introduce detailed simulated images that have been developed using shapelets, an orthogonal

[1] Institute of Astronomy, Madingley Road, Cambridge CB3 0HA, UK; rjm@ast.cam.ac.uk.
[2] Department of Astronomy, 105-24, California Institute of Technology, 1201 East California Boulevard, Pasadena, CA 91125.
[3] Laboratory for Astronomy and Solar Physics, Code 681, NASA Goddard Space Flight Center, Greenbelt, MD 20771.
[4] NASA/NRC Research Associate.
[5] Current address: Service d'Astrophysique, CEA Saclay, F-91191 Gif-sur-Yvette, France.
[6] Institute for Astronomy, University of Edinburgh, Blackford Hill, Edinburgh EH9 3HJ, UK.
[7] Department of Physics and Astronomy, University of Pennsylvania, 209 South 33rd Street, Philadelphia, PA 19104.
[8] Department of Astronomy, 830 Dennison Building, University of Michigan, Ann Arbor, MI 48109.
[9] Lawrence Berkeley National Laboratory, 1 Cyclotron Road, Berkeley, CA 94720.

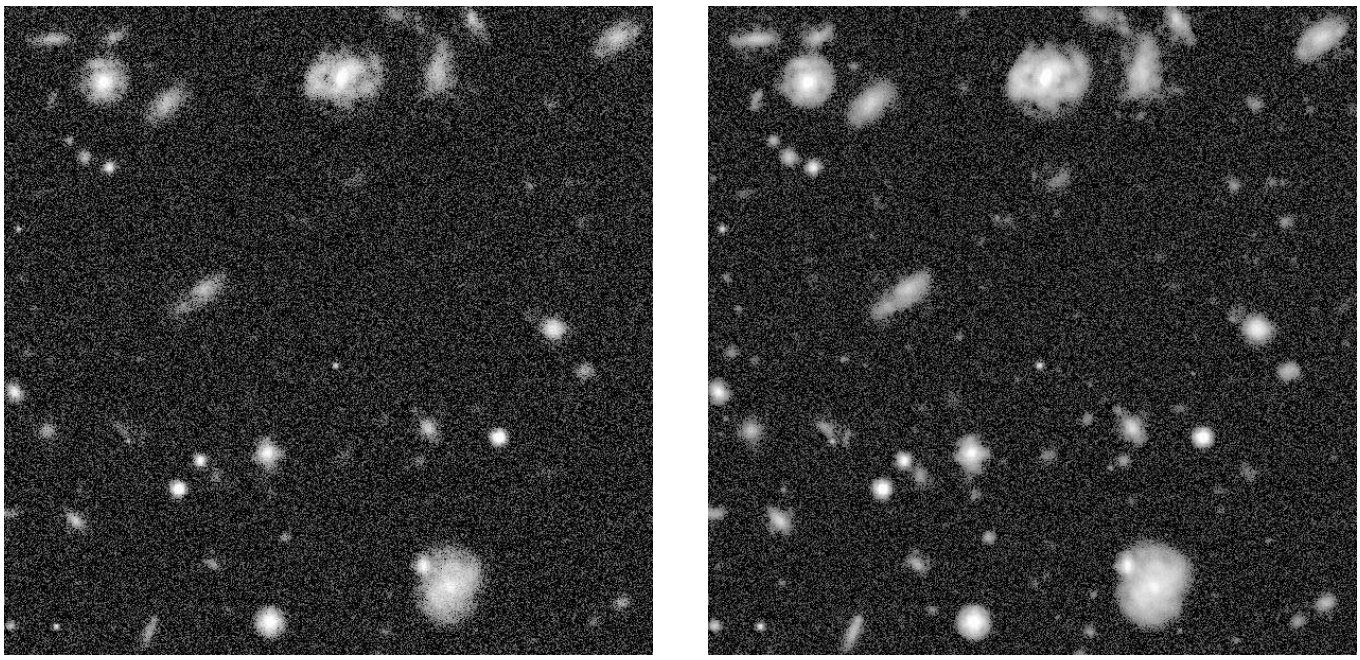

FIG. 1.—Size $30'' \times 30''$ portions of simulated *SNAP I*-band images, using the PSF shown in Fig. 2. *Left*, to the depth of the proposed *SNAP* wide survey; *right*, to the depth of the Hubble Deep Fields. The *SNAP* deep survey will be some 2 mag deeper than the latter, but further real data from the ACS on *HST* are needed to simulate this depth accurately.

parameterization of galaxy shapes (Refregier 2003a; Massey et al. 2004). The simulated images contain realistic populations and morphologies of galaxies as will be seen from space, modeled from those in the Hubble Deep Fields (HDFs; Williams et al. 1996, 1998). These shapelet galaxies can be artificially sheared to simulate gravitational lensing. The subsequent recovery accuracy of the known input shear is discussed in § 3. We discuss the accuracy of *SNAP* photometric redshifts in § 4. These two measurements are combined to predict the accuracy of projected dark matter maps, three-dimensional dark matter maps, and mass-selected cluster catalogs in § 5. We draw conclusions in § 6. Our results are used to predict the accuracy of cosmological parameter constraints in Refregier et al. (2004, hereafter Paper III).

2. IMAGE SIMULATIONS

In this section, we describe our method for simulating realistic images, aiming to closely resemble images observed with a space-based telescope. These simulations are part of a full pipeline that allows us to propagate the effects of perturbations in the instrument design onto shear statistics and cosmological parameters. Example simulated images are shown in Figure 1.

2.1. *Procedure*

The shapelet formalism (Refregier 2003a; Refregier & Bacon 2003; summarized in § 2.2) has been used to model all the galaxies in the HDFs. Using just a few numbers, this parameterization captures the detailed morphology of the galaxies, including spiral arms, arbitrary radial profiles, and irregular substructure. The parameters for each galaxy are stored in a multidimensional parameter space. This is then randomly resampled, to simulate new and unique galaxies with realistic properties as compared with those in the original HDFs. A detailed description of the simulation procedure and performance can be found in Massey et al. (2004).

The simulated images are built up with galaxies of all types (spiral, elliptical, and irregular) in their observed proportions, with realistic number counts and a size distribution reproducing that in the HDFs. Their morphology distribution as a function of magnitude also reproduces that in the HDFs. Most importantly, all these objects possess a precisely known shape, magnitude, size, and shear. The amount of shear can be adjusted in shapelet space as an input parameter.

Observational effects including PSF convolution, pixelization, noise, and detector throughput are then incorporated in the simulations. In § 2.3, we describe the engineering specifications we have used to emulate the performance of the *SNAP* satellite. In § 3 we then attempt to recover the known input shear from these realistic, noisy images using existing (and independent) shear-measurement methods.

2.2. *Shapelets*

Here we briefly describe the idea of shapelets, which is at the core of our image simulation package. More comprehensive details are available in Refregier (2003a), Refregier & Bacon (2003), and Massey et al. (2004). Shapelets are an orthonormal basis set of two-dimensional Gauss-Hermite functions. They can be used to model any localized object by building up its image as a series of successive basis functions, each weighted by a "shapelet coefficient," rather like a Fourier or wavelet transform. Each polar basis state and shapelet coefficient can be identified by two integers: $n \geq 0$ describing the number of radial oscillations, and $m \in \{-n, n\}$ the azimuthal oscillations, or rotational degrees of symmetry. The basis is complete when the series is summed to infinity, but it is truncated in practice at a finite $n_{\max}$. This offers image compression because an object is typically well modeled using only a few shapelet coefficients.

Conveniently, the shapelet coefficients are Gaussian-weighted multipole moments (with the rms width of the Gaussian known as the shapelet scale size β), as commonly

used in various astronomical applications. The $n = 2$ states are thus Gaussian-weighted quadrupole moments, the $n = 4$ states octopole moments, etc. Shapelet basis functions also happen to be eigenstates of the two-dimensional quantum harmonic oscillator, with n and m corresponding respectively to energy and angular momentum quantum numbers. This analogy suggests a well-developed formalism. For instance, shears and dilations can be represented analytically as $\hat{a}$ or $\hat{a}^{\dagger}$ ladder operators (Refregier 2003a), and PSF convolutions as a trivial bra-ket matrix operation (Refregier & Bacon 2003).

Massey et al. (2004) demonstrates how HDF galaxies can be represented as shapelets and then transformed by slight adjustments of their shapelet coefficients into new shapes. This process produces genuinely new but realistic galaxies, as proved by the similar distributions in HDF and simulated data of commonly used diagnostics from SExtractor (Bertin & Arnouts 1996) and galaxy morphology packages (e.g., Conselice, Bershady, & Jangren 2000).

2.3. *SNAP Simulations*

For this work, our image simulations have been tuned to the instrument and specifications of the proposed *SNAP* mission (Paper I; Aldering et al. 2002; Kim et al. 2002; Lampton et al. 2002, 2003).[10] The *SNAP* strategy includes a wide, 300 deg^2 survey (with 4×500 s exposures reaching a depth of AB magnitude 27.7 in R for a point source at 5 σ), and a deep, 15 deg^2 survey ($120 \times 4 \times 300$ s to AB 30.2). For an exponential disk galaxy with FWHM = 0.″12, these limits become 26.6 and 28.9, respectively.

The predicted *SNAP* PSF at the middle of the illuminated region of the focal plane is illustrated in Figure 2. Following the analysis of Paper I, this was obtained for the current satellite design, using ray tracing, aperture diffraction, and CCD diffusion. In this paper we also illustrate the decomposition of the *SNAP* PSF into shapelets. As shown in the top panel of Figure 2, our model includes the second diffraction ring and is accurate to nearly 1 part in 10^3. It does not include much of the extended low-level diffraction spikes, which we ignore. Convolution with this residual PSF pattern adds less than 0.7% to the ellipticity of any exponential disk galaxy that passes the size cut into the lensing catalog (see § 3.2). Given the further factor of G^{-1} in equation (4), to convert ellipticity into shear, this residual thus has a negligible impact upon shear measurement within the accuracy of the current methods.

Simulated images used to calibrate the shear-measurement method (see § 3.2) were first sheared and then convolved with the full *SNAP* PSF shown in Figure 2. For this application, it is essential that the shearing be applied before the smearing, just as occurs in the real universe. Shear-measurement methods have been designed to correct for precisely this sequence of events. However, our simulated galaxies were modeled on real HDF objects, which had already been naturally convolved with the Wide Field Planetary Camera 2 (WFPC2) PSF when the HDF images were taken. Consequently, our simulated objects in § 3.2 exhibit smoothing from both a circularized WFPC2 PSF (plus shearing) and a *SNAP* PSF. This double PSF artificially reduces the rms ellipticity of galaxies by approximately ~2% and increases the size of a point source by 22%. One should note that the first PSF convolution occurs, and the galaxy orientations are randomized, before shearing. This effect therefore corresponds to a small alteration in the intrinsic shape distribution of galaxies, but it does not bias the shear measurement (see discussion in Massey et al. 2004).

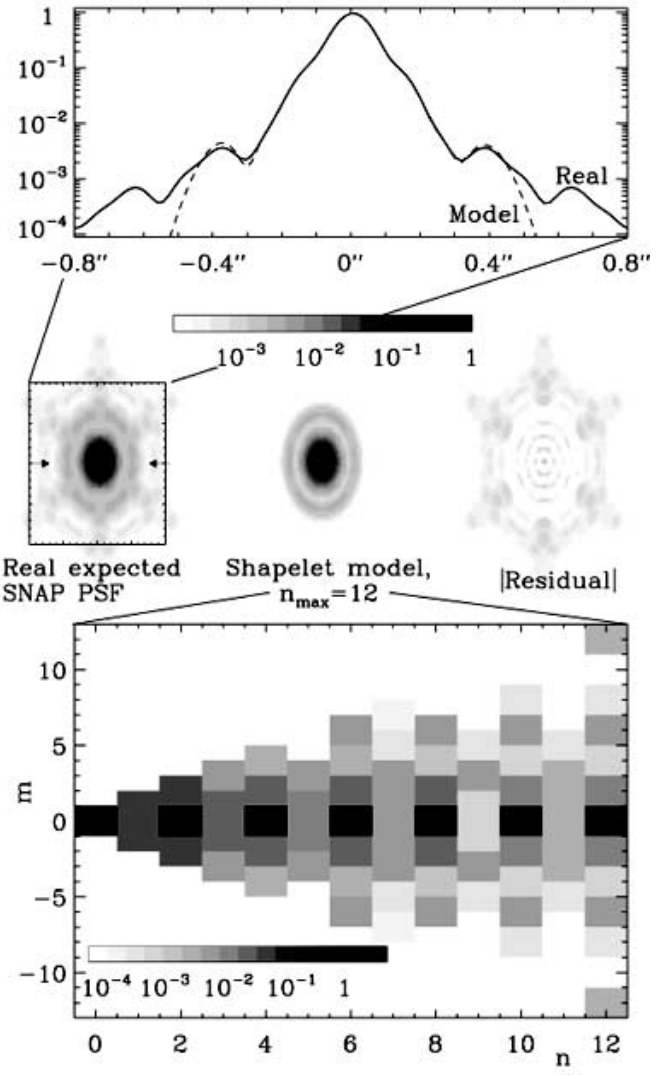

FIG. 2.—Shapelet decomposition of the proposed *SNAP* PSF. *Top*, a horizontal slice through the center of the real (*solid line*) and shapelet-reconstructed (*dashed line*) PSF; *middle*, in two dimensions, the real PSF, its recovery using shapelets, and the residual difference between the two, from left to right; *bottom*, moduli of the corresponding polar shapelet coefficients with order up to $n_{max} = 12$. Note that all intensity scales are logarithmic. The circular ($m = 0$) core is modeled to an accuracy of about 10^{-3}, and the beginnings of sixfold symmetric structure are seen as power in the $m = \pm 6, \pm 12$ shapelet coefficients.

Simulated images used to predict the lensing efficiency as a function of exposure time (see § 3.3) were produced differently. For these, we needed to ensure realistic size distributions and number counts in the simulations. The galaxies had no artificial shear added: they just have a scatter of ellipticities due to their own intrinsic shapes. We convolved these galaxies by the PSF difference between the *Hubble Space Telescope* (*HST*) and *SNAP*. This is obtained by deconvolving the WFPC2 PSF from the *SNAP* PSF model, in shapelet space. Smoothing an object with this smaller kernel is enough to convert it from an observation with *HST* to one with *SNAP*, although without inputting shear.

Example simulated images are shown in Figure 1 for the wide *SNAP* survey (*left*) and to the depth of the HDFs (*right*). They include a noise model consisting of both photon counting error and a Gaussian background. These compare well with real deep

[10] See also http://snap.lbl.gov.

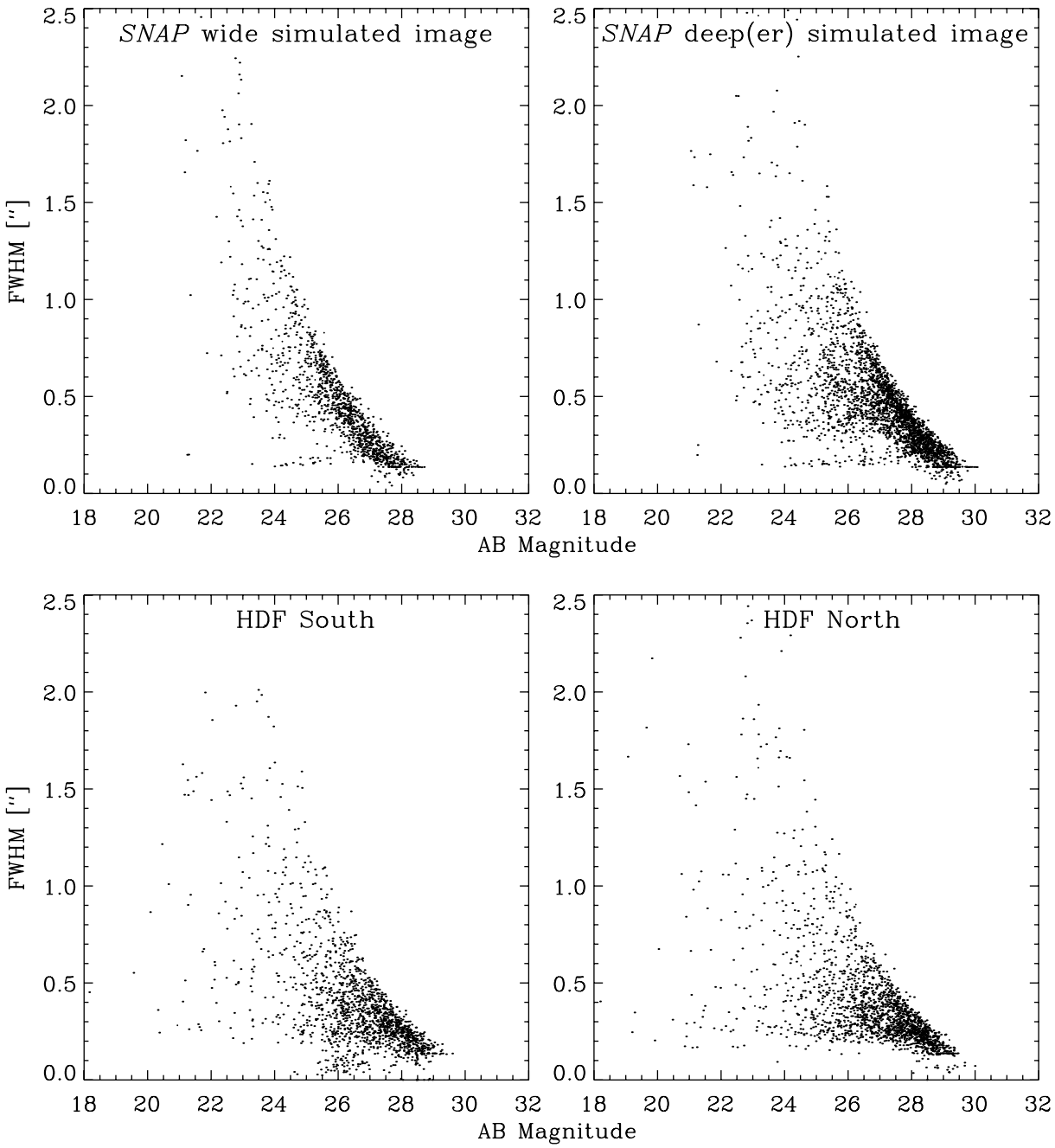

FIG. 3.—Size vs. magnitude as determined by SExtractor with an S/N cutoff at $\nu = 1.5$. The top panels are for simulated *SNAP* *I*-band images of the same size as the HDFs. For reference, the bottom panels are of the HDFs themselves using the same SExtractor parameters.

HST images (see Massey et al. 2004). The *SNAP* deep fields will be about 2 magnitudes deeper than the HDFs. However, deeper surveys with the Advanced Camera for Surveys (ACS) on board *HST* are awaited to accurately model galaxies at this depth. Figure 3 shows the size-magnitude distribution of the simulated images to both depths (*top*). Again, the simulations reproduce the statistics of the real HDFs (*bottom*).

2.4. *Limitations of the Simulations*

The *SNAP* wide-survey strategy includes four dithered exposures at each pointing. This will enable the removal of cosmic rays and, if necessary, the simultaneous measurement of instrumental distortions. Because of the high orbit and slow thermal cycle, instrument flexure and the PSF are expected to be very stable (see Paper I). It should therefore be possible to map internal distortions and compensate for them even on small scales, using periodic observations of stellar fields. Consequently, neither cosmic rays nor astrometric distortions are added to the simulations.

The *SNAP* CCD pixels are 0.″1 in size and thus undersample the PSF. To compensate for this, the dithered exposures will be stacked, as usual for *HST* images, using the Drizzle algorithm (Fruchter & Hook 2002). Alternatively, galaxy shapes may be fitted simultaneously from several exposures. Drizzle recovers some resolution, and will be particularly effective for the multiply imaged *SNAP* deep survey, but has the side effect of aliasing the image and correlating the noise in adjacent pixels. We have not yet included this entire pipeline in the

simulations but merely implemented a smaller pixel scale and model background noise that is higher in each pixel (although uncorrelated). Following the example of the HDF final data reduction, we choose 0.″04 pixels. Unfortunately, the detection and shape measurement of very faint galaxies are sensitive to the precise noise properties of an image. Because of these instabilities, our simulated images are only reliable down to approximately $I \simeq 29.5$ (see Massey et al. 2004). This is just below the magnitude cut applied by our shear-measurement method at $I = 29.1$. A further investigation will include full use of Drizzle and more detailed noise models. This will also address the issue of pointing accuracy and consider the consequences of "dead zones" around the edges of the pixels that house the CCD electronics and are therefore unresponsive to light.

The image simulations are based upon the galaxies in the HDF, which is itself a special region of space selected to contain no large or bright objects. As a result, our simulations do not yet include these either. The source catalog is being expanded as ACS data from the Great Observatories Origins Deep Survey become publicly available.

The image simulations are currently monochromatic, in the *HST* F814W (hereafter I) filter. Since gravitational lensing is achromatic, shear measurement can be performed in any band; indeed, all tested shear-measurement methods so far use only one color at a time. The I or R band is typically chosen for shear measurement because of the increased galaxy number density, advanced detector technology, and small PSF at these wavelengths. Surveys such as COMBO-17 (Brown et al. 2003) and VIRMOS-DESCART (van Waerbeke et al. 2002) are leading a trend to use additional multicolor photometry to provide photometric redshifts of the source galaxy population. The *SNAP* surveys will be simultaneously observed in nine bands: six optical colors spanning roughly B through I, plus J, H', and K (the near-IR filters are twice as large and receive double the total exposure times given in § 2.1; see Paper I). We have not simulated this multicolor data, but it will inevitably raise the signal-to-noise ratio (S/N) of shear estimation for every source galaxy. At a minimum, image co-addition or simultaneous fits to shapes in several colors will increase the effective exposure time. Something more ambitious, such as shifting to the rest-frame R or the rotating disk disalignment suggested by Blain (2002), might even reduce systematic measurement biases. Further work is needed in cosmic shear methodology to investigate the optimal use of multicolor data. However, it can already be said that our current monochromatic approach will yield a conservative estimate of the lensing sensitivity expected from future analyses.

3. WEAK-LENSING SENSITIVITY

In this section, we determine the accuracy with which it is possible to recover the input shear from the noisy-image simulations. The formalism of shapelets can be used to form an accurate shear measurement (Refregier & Bacon 2003). However, since the images themselves were created using shapelets, we choose here to be conservative and use a slightly older but independent method developed by Rhodes, Refregier, & Groth (2000, hereafter RRG).

3.1. *Advantages of Space*

We first discuss the advantages specific to weak-lensing measurement that are provided by observations from space. The figure of merit for any lensing survey needs to include more than the *étendue*, a product of the survey area and the flux-gathering power of a telescope (Tyson 2002; Kaiser et al. 2002).[11] It must also account for the finite PSF size, the size-magnitude distribution of background galaxies, and systematics (e.g., due to the atmosphere or telescope optics). Shear sensitivity is raised for a spacecraft over a ground-based telescope for the additional reasons listed below.

1. More objects have measurable shapes. Although not as much sky area will be surveyed as by proposed ground-based surveys such as MegaCam (Boulade et al. 2000), VISTA,[12] or LSST,[13] the number density of resolved objects is an order of magnitude higher from space (compare Fig. 5 with Tables 2–4 of Bacon et al. 2001). Such an increase in S/N per unit area will enable the mapping of projected dark matter maps with adequate resolution for a direct comparison with redshift surveys (§ 5.1) and the generation of a mass-selected cluster catalog (see, e.g., Weinberg & Kamionkowski 2002; Hoekstra 2003). Quantitative study of high-sigma mass fluctuations is one of the most promising methods to break degeneracies in cosmological parameter estimation, in particular, constraining Ω_m (see, e.g., Bernardeau et al. 1997; Cooray et al. 2000; Munshi & Jain 2001; Schneider et al. 2002). Furthermore, studying well-resolved groups and clusters individually, rather than statistically, will lead to a better understanding of astrophysical phenomena such as biasing and the mass-temperature relation (Huterer & White 2002; Smith et al. 2003; Weinberg et al. 2004).

2. The shapes of individual galaxies are more precisely measured. The *SNAP* PSF is small (0.″13 FWHM, assuming 4 μm CCD diffusion). It is more isotropic and, importantly, more stable than even the *HST* PSF (see Paper I). This enables shape measurement to be more reliable, or possible at all, for small, distant galaxies. The stable photometry from the 3 day orbit may even permit the use of weak lensing magnification, as well as shear information (see, e.g., Jain 2002). Whether directly measured or inferred from shear, this in turn is useful to correct for the effect of lensing on the distance moduli to the *SNAP* supernovae (Dalal et al. 2003).

3. Galaxy redshifts are known accurately and to a greater depth. *SNAP*'s stable nine-band optical and near-IR imaging is ideal to produce exquisite photometric redshifts (photo-z's) for almost all galaxies at $z \lesssim 3$ detected at 5 σ in the I band (see § 4). This should be compared with the ~38% completeness of photo-z's possible from the ground in the COMBO-17 data with a similar cut and a median redshift of $R \simeq 24$ (Brown et al. 2003). This allows a good estimation of the redshift distribution of source galaxies, the uncertainty in which is a major contribution to the error budget in current lensing surveys. Projected two-dimensional power spectra and maps can be drawn in several redshift slices, using redshift tomography. More ambitiously, cluster catalogs and dark matter maps can be constructed directly in three dimensions (§ 5.2), enabling the three-dimensional correlation of mass and light and the tracing of the growth of mass structures.

4. Galaxies are farther away. Distant objects, too faint and too small to be seen from the ground, are measurable from space. The evolution of structures can thus be traced from earlier epochs, giving a better handle on cosmological parameters (see Paper III). Furthermore, recent numerical simulations (Jing 2002; Hui & Zhang 2002) suggest that intrinsic galaxy alignments affect lensing surveys to a greater depth in redshift

[11] Available at http://panstarrs.ifa.hawaii.edu/public/documents/poi_book.pdf and http://www7.nationalacademies.org/bpa/LSST.pdf, respectively.

[12] See http://www.vista.ac.uk.

[13] See http://www.lsst.org.

than previously assumed. If this is confirmed, intrinsic alignments will mimic and bias cosmic shear signal in all but the deepest surveys, where the galaxies are farther apart in real space. Using three-dimensional positions of galaxies from *SNAP* photo-z's, it will be possible to isolate close galaxy pairs and to measure their alignments, or to optimally down-weight close pairs and thus reduce their impact (Heavens & Heymans 2003; King & Schneider 2003).

3.2. *Shear-Measurement Method*

The advantages of space-based data described above will provide limited gains without an equally precise and robust shape-measurement method. The now standard weak-lensing method for ground-based data was introduced by Kaiser, Squires, & Broadhurst (1995, hereafter KSB). KSB form shear estimators from quadrupole and octopole moments of an object's flux. Modern techniques are being developed to incorporate higher order shape moments or Bayesian statistics to raise the sensitivity to shear. These methods include shapelets (Refregier & Bacon 2003) and others by Bernstein & Jarvis (2002), Bridle et al. (2004), and Kaiser (2000). However, since the simulations themselves were created using shapelets, we choose here to be conservative and use the independent method developed by RRG. This is related to KSB but optimized for use with space-based data. It has already been used extensively on *HST* images (Rhodes, Refregier, & Groth 2001; Refregier, Rhodes, & Groth 2002) and is therefore appropriate for our current purposes.

Following KSB, RRG measure a galaxy's two-component ellipticity ϵ_i from the Gaussian-weighted quadrupole moments of its surface brightness $I(\theta)$,

$$\epsilon_i \equiv \frac{\{J_{11} - J_{22}, 2J_{12}\}}{J_{11} + J_{22}}, \tag{1}$$

where

$$J_{ij} \equiv \frac{\int d^2\theta\, \theta_i \theta_j w(\theta) I(\theta)}{\int d^2\theta\, w(\theta) I(\theta)} \tag{2}$$

and $w(\theta)$ is a Gaussian of width adjusted to match the galaxy size. The unweighted PSF moments are measured from a (simulated) star field, and the RRG method corrects the galaxy ellipticities to first order for PSF smearing. Occasional unphysical ellipticities, $|\epsilon| > 2$, are excluded, along with galaxies fainter than AB magnitude 26.5 (for the *SNAP* wide survey) or AB 29.1 (for the *SNAP* deep survey) and with sizes

$$R \equiv \sqrt{\tfrac{1}{2}(J_{11} + J_{22})} \leq 1.7 \text{ pixels}. \tag{3}$$

Note that R is an rms size measure rather than a FWHM, and that this procedure does indeed select only resolved objects. The locations of these cuts have been chosen to yield reasonably stable results; the effect of moving the size cut is discussed further in section § 3.4.

The RRG method finally provides the shear susceptibility conversion factor, G, to generate unbiased shear estimators $\hat{\gamma}_i$ for an ensemble of objects, given by

$$\hat{\gamma}_i = \langle \epsilon_i \rangle / G, \tag{4}$$

where G depends on the fourth-order moments J_{ijkl} of a galaxy population, defined similarly to equation (2). In our simulated *SNAP* images, G is of order 1.6.

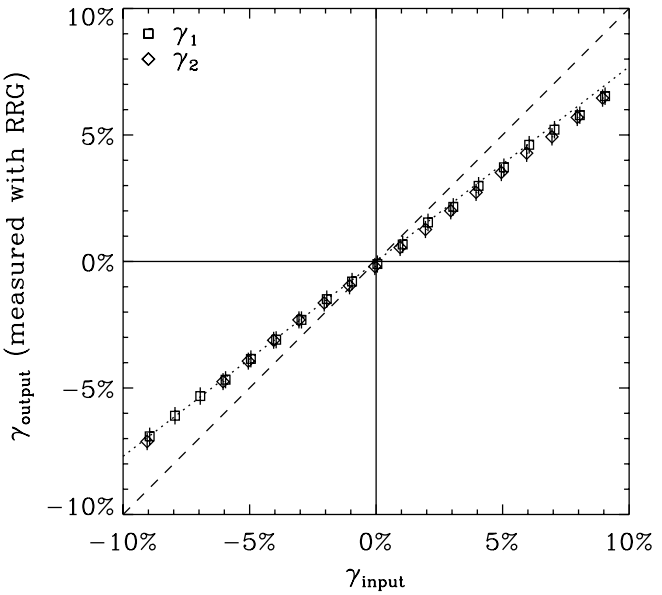

FIG. 4.—Applied shear γ_{in} in the shapelet simulated images vs. its recovery γ_{out} using an independent measurement method (Rhodes et al. 2000). The image used is one 7.5 arcmin^2 realization of the *SNAP* deep survey shown in Fig. 6. The recovery is linear, but the slope of the fitted line (*dotted line*) is flatter than that expected (*dashed line*).

This shear-measurement method and the simulations are tested in Figure 4. An artificial shear is applied uniformly upon all objects in a 7.5 arcmin^2 simulated image, in the $\gamma_2 = 0$ and $\gamma_1 = 0$ directions, before convolution with the *SNAP* PSF. Using RRG, we correct for the PSF smearing and recover the input shear. As can be seen in Figure 4, the recovery is linear, but the slope (*dotted line*) is underestimated (*dashed line*). This inconsistency probably has two origins: inaccuracy of the image simulations and instabilities in the shear-measurement method. The latter may be removed with future techniques. For the purposes of this paper, we follow the procedure adopted by Bacon et al. (2001), where a similar bias was observed in the KSB method. We apply a linear correction factor to the measured shears and to their errors. This factor is $(0.79 \pm 0.03)^{-1}$ at the depth of the HDFs, and $(0.87 \pm 0.04)^{-1}$ for the *SNAP* wide survey.

Even after this correction, there remains a small difference in the rms scatter of galaxy ellipticities between the simulations and real data from the Groth strip (Rhodes et al. 2001). As shown in Massey et al. (2004), this discrepancy is not detected with the standard shape measures of SExtractor (Bertin & Arnouts 1996); however, RRG proves to be a more sensitive test. Perhaps because of the precise properties of the background noise, or perhaps because the wings of simulated objects are truncated beyond the SExtractor isophotal cutoffs, σ_e is observed by RRG to be lower in the simulated images by another factor of $\sim$0.8. Work is in progress to establish the origin of this effect. For the purposes of this paper, we simply increase the error bars by this amount.

3.3. *Shear Sensitivity of SNAP*

Now that the image simulation and analysis pipeline is in place, we can measure *SNAP*'s sensitivity to shear. Trade-off studies are under way for several alternative telescope designs, including the level of CCD charge diffusion, the pixel size, the effect of drizzling, and the coefficient of thermal expansion in the secondary struts, which may be the main cause of temporal

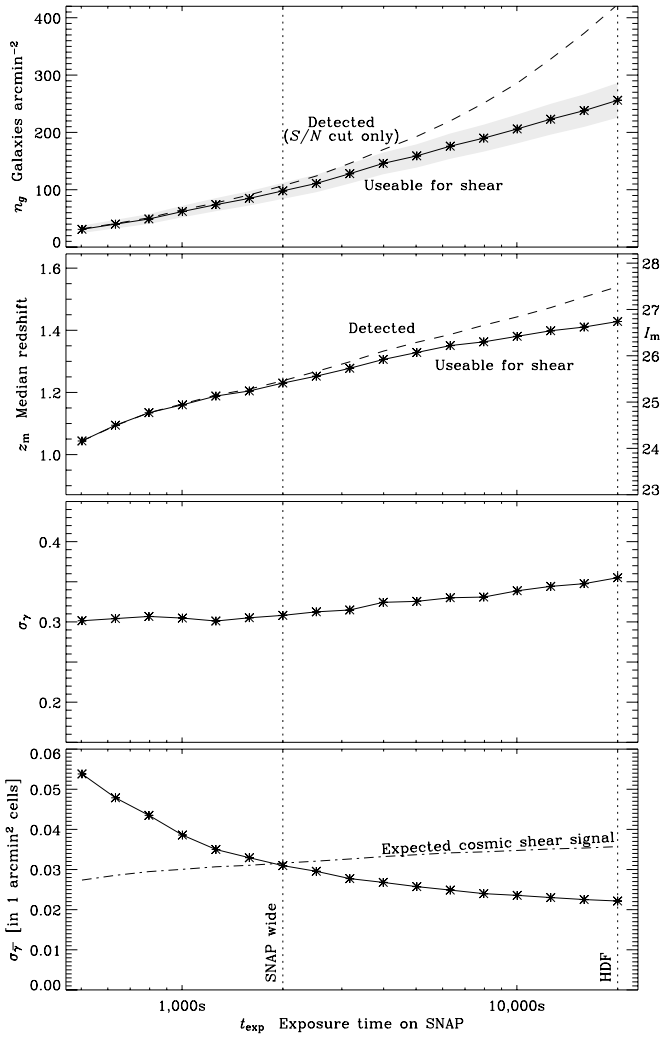

FIG. 5.—Shear sensitivity as a function of *SNAP* exposure time $t_{\rm exp}$. *Top*: Surface number density of all galaxies ($n_{g,\rm tot}$) detected by SExtractor and of the subset (n_g) of these usable for weak lensing, i.e., having survived further cuts in size and ellipticity by the RRG method (see text). *Second from top*: Median *I*-band magnitude, I_m, in the two subsets of the galaxy catalog, which has been interpreted as median redshift, z_m, using eq. (8). *Second from bottom*: The rms error $\sigma_\gamma = \langle|\gamma|^2\rangle^{1/2}$ per galaxy for measuring the shear γ, after PSF correction and shear calibration. *Bottom*: The rms error $\sigma_{\bar\gamma}$ for measuring the mean shear $\bar\gamma$ in 1 arcmin^2 bins. The dot-dashed line shows an estimate of the expected rms shear in a ΛCDM universe.

variation in the PSF (see Paper I). Here we present the results of a study that uses the baseline design specifications and time-averaged PSF of the *SNAP* satellite. In this study the PSF used is the residual between the *HST* and *SNAP* PSFs (see § 2.3), in order to keep the size distribution of galaxies realistic for *SNAP* images.

The top panel of Figure 5 shows the surface number density n_g of galaxies in a survey of a given exposure time $t_{\rm exp}$ on *SNAP*. The exposure times reflect a ∼5 times overall improvement in instrument throughput and detector efficiency over WFPC2 on *HST* (Lampton et al. 2002). The dashed line shows the number density $n_{g,\rm tot}$ of all the galaxies detected by SExtractor, after an S/N cut that is equivalent to $I < 29.1$ at the depth of the HDFs. As discussed in § 3.2, galaxies that are too faint, too small, or too elliptical are excluded from weak-shear catalogs. The solid line shows the number density n_g of galaxies that are usable for weak lensing following the magnitude, size, and ellipticity cuts. The error bars reflect the uncertainty in measuring number counts at low S/N and an estimated sample variance between the HDF-N and HDF-S.

An important cut in the weak-lensing analysis is the size cut, which reduces the detected galaxy sample by about 30% at the depth of the HDFs. This fraction is a strong function of PSF size and is thus much larger for ground-based imaging. As can be inferred from the top panel of Figure 5, the *SNAP* wide survey ($n_g \simeq 100$ galaxies arcmin^{-2}) will thus provide a dramatic improvement over current ground-based surveys ($n_g \sim 25$ galaxies arcmin^{-2} is used by most groups; see, e.g., Bacon et al. 2003). The effect of moving the size cut is discussed further in § 3.4.

The second panel of Figure 5 shows the median magnitude, I_m, of the galaxy catalog before and after cuts in size and ellipticity by the weak-lensing analysis software. This has been converted to a median redshift, z_m, using equation (8) below. For the purposes of this plot, we assume that this relationship is still valid even after the size cut.

The third panel of Figure 5 shows the rms error $\sigma_\gamma = \langle|\gamma|^2\rangle^{1/2}$ per galaxy for measuring the shear, after the PSF correction and shear calibration. The slightly increasing error at longer $t_{\rm exp}$ reflects the decreasing size of fainter galaxies and correspondingly less resolved information content available about their shapes. To map the shear, the noise can be reduced by binning the galaxies into cells. The rms noise of the shear $\bar\gamma$ averaged in a cell of solid angle $A = 1$ arcmin^2 is given by

$$\sigma_{\bar\gamma} \simeq \sigma_\gamma / \sqrt{n_g A} \qquad (5)$$

and is plotted in the bottom panel of Figure 5. The wide and deep *SNAP* surveys will thus afford a 1 σ sensitivity for the shear of ≃3.0% and better than 2.2% on this scale, respectively. As a comparison, the rms shear expected from lensing on this scale in a cold dark matter model with a cosmological constant (ΛCDM) is approximately 3% (assuming $\Omega_m = 0.3$, $\Omega_\Lambda = 0.7$, $\sigma_8 = 0.9$, and $\Gamma = 0.21$). This signal increases with survey depth because the total lensing along a line of sight is cumulative. The wide *SNAP* survey will thus be ideal to map the mass fluctuations on scales of 1 arcmin^2, with an average S/N of unity in each cell. The recovery of simulated mass maps will be discussed in § 5.

Note that the shear sensitivities presented here are conservative estimates, particularly for the deep *SNAP* survey. The image simulations extend so far only to the depth of the HDFs. Future shear-measurement methodology will also be more accurate and stable on any individual, resolved galaxy than the RRG method used in this paper. Higher order shape statistics (e.g., shapelets) will be used, as will simultaneous measurements in multiple colors and preselection of early-type galaxy morphologies.

3.4. *Effect of Size Cut and Pixel Scale*

Small, faint, and highly elliptical objects are excluded from the final galaxy catalog in the RRG shear-measurement method. Of all these cuts, it is the size cut that excludes the most objects. In an image at the depth of the HDFs, about 30% of detected galaxies are smaller than our adopted size cut at $R = 1.7$ pixels. The exact position of this cut has been determined empirically to produce stable results, from experience with both *HST* data and our simulated images. The quantitative effects of moving the size cut are demonstrated in Figure 6.

If the cut is moved to a larger size, fewer objects are allowed into the final galaxy catalog, and the shear field is sampled in fewer locations. Consequently, both dark matter

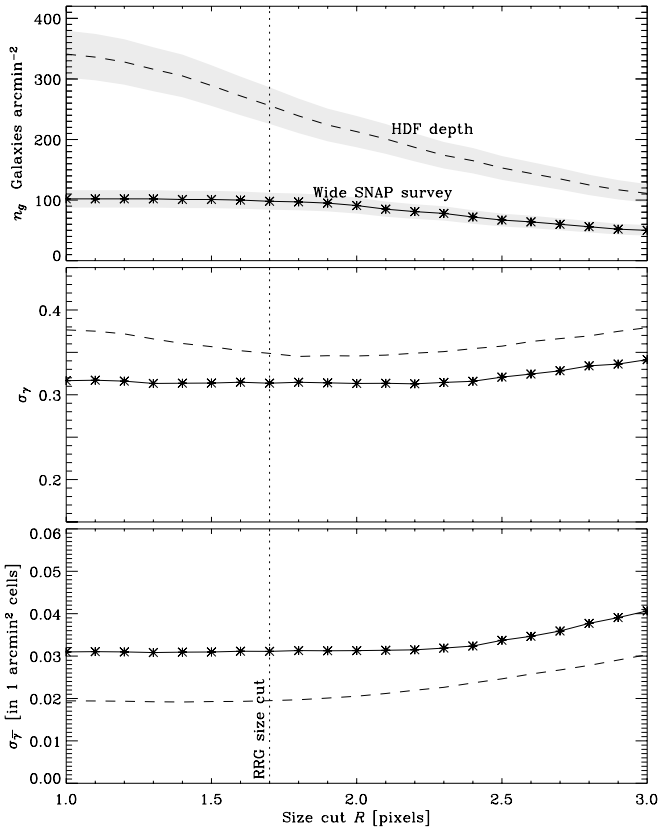

FIG. 6.—Shear sensitivity as a function of size cut R in the RRG shape-measurement method for the wide *SNAP* survey (*solid lines*) and at the depth of the HDFs (*dashed lines*). The vertical dotted line shows the fiducial value adopted elsewhere in our analysis. *Top*, surface number density of galaxies usable for weak lensing; *middle*, rms error $\sigma_\gamma = \langle|\gamma|^2\rangle^{1/2}$ per galaxy for measuring the shear γ, after PSF correction and shear calibration; *bottom*, rms error for measuring the mean shear $\bar{\gamma}$ in 1 arcmin^2 bins.

maps and cosmic shear statistics become more noisy. If smaller galaxies are included in the catalog, the shear field is indeed better sampled, but the shape-measurement error is worse on these galaxies. The bottom panel of Figure 6 shows that moving the size cut to smaller objects yields no net change in the precision of shear recovery: adding noisy shear estimators to the catalog neither improves nor worsens the measurement. A size cut at $R = 1.7$ pixels is optimal at the depth of the HDFs and in the observing conditions modeled by our image simulations. To simplify comparisons of galaxy number density, the same cut has been applied to data at the depth of the *SNAP* wide survey. A different cut could have been adopted, producing fewer galaxies but each with more-accurate shear estimators: the crucial figure $\sigma_{\bar{\gamma}}$ would not change. (This is especially true in the *SNAP* wide survey, because of the relative dearth of small galaxies.)

As described in § 2.4, we have assumed that an effective image resolution of 0.″04 can be recovered for *SNAP* data by taking multiple, dithered exposures, and either stacking them with the Drizzle algorithm or fitting each galaxy's shape simultaneously in them all. The increase in image resolution from these techniques is vital for cosmic shear measurements. The number density of usable galaxies increases dramatically, and the measurement of their shapes is improved. Were it not possible to apply Drizzle or to recover this resolution, the large pixel scale currently proposed for *SNAP* would seriously impair shear measurement. A size cut at $R = 0.''12$ (=3 pixels in Fig. 6) would roughly halve the number density of usable sources and correspondingly reduce the sensitivity to gravitational lensing.

4. PHOTOMETRIC REDSHIFT ACCURACY

Gravitational lensing is achromatic, so shear measurement may be performed in any color. As discussed in § 2.4, current techniques measure galaxy shapes in only one band at a time (usually R or I is chosen, for their steeper slope of number counts). However, gravitational lensing is also a purely geometric effect, and measurements are aided greatly by accurately knowing the distances to sources. The latest surveys, and future high-precision measurements, will therefore require multiple colors for photometric redshift estimation. Reliable photo-z's will not only remove current errors due to uncertainty in the redshift distribution of background sources but even make possible an entirely three-dimensional mass reconstruction, as demonstrated in § 5.2, Taylor (2001), Hu & Keeton (2002), Bacon & Taylor (2003), and Jain & Taylor (2003).

SNAP's thermally stable, 3 day long orbit is specifically designed for excellent photometry on supernovae. Combining all nine broadband filters (six optical, three near-IR) will also provide an unprecedented level of photo-z accuracy, for all morphological types of galaxies over a large range of redshifts. In this section, we simulate *SNAP* photometric data in order to determine this precision.

We have used the "hyperz" code (Bolzonella, Miralles, & Pelló 2000) to generate the observed magnitudes of a realistic catalog of galaxies following Lilly et al. (1995),

$$\frac{dN(I)}{dI} \simeq 10^{0.35I}, \tag{6}$$

where I is the I-band magnitude. The galaxies were assigned a distribution of spectral energy distribution (SED) types similar to that in real data and containing elliptical, spiral, and starburst galaxies. Redshifts were assigned at random, and independently of spectral type, according to Koo et al. (1996) as verified by the DEEP Collaboration,[14]

$$\frac{dN(z)}{dz} \simeq z^2 e^{-(z/z_m)^2}, \tag{7}$$

where

$$z_m = 0.722 + 0.149(I - 22.0) \tag{8}$$

(Lanzetta, Yahil, & Fernández-Soto 1996). *SNAP* colors were then inferred by integrating the SED across filter profiles, adding an amount of noise corresponding to the exposure time and instrument throughput.

Hyperz was then used again, to estimate redshifts for the simulated catalog as if it were real data. Unlike the image simulations in § 2, this approach can already be taken to the depth of both the wide and the deep *SNAP* surveys by extrapolating functional forms for the luminosity and redshift distributions (eqs. [6] and [7]). Magnitude cuts were applied at AB 26.5 (wide) or AB 29.1 (deep) in R. Similar magnitude cuts were made in each filter, chosen at the 10 σ detection level of an exponential disk galaxy with FWHM = 0.″12 (Kim et al. 2002). Past experience with lensing data (see § 3.2 and Bacon et al. 2001) confirms that this is reasonable S/N limit. Note however that the size and ellipticity cuts implemented for the simulated images in § 3.2 were not included at this stage.

[14] See http://deep.ucolick.org.

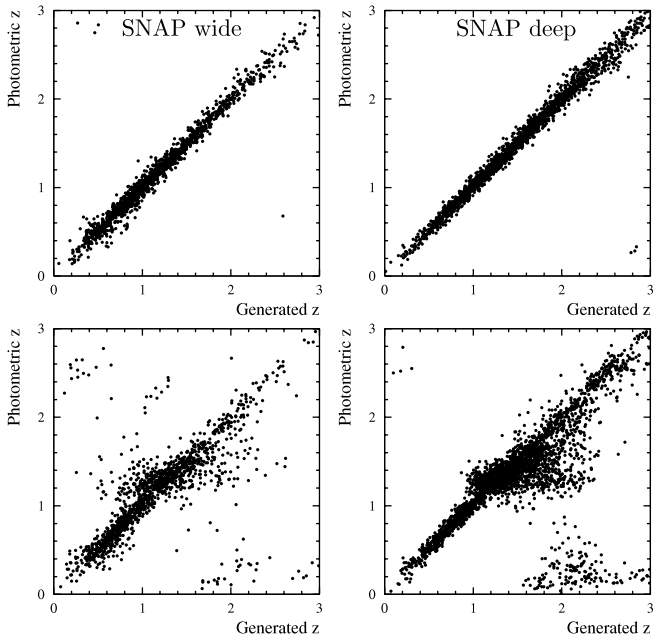

FIG. 7.—Recovery of redshifts of a realistic population of galaxies using "hyperz" with the *SNAP* filter set. *Top left*, the wide survey, using all nine colors; *top right*, the deep survey using all nine colors; *bottom*, the same, but with only the six optical colors, as if the near-IR HgCdTe data were not available.

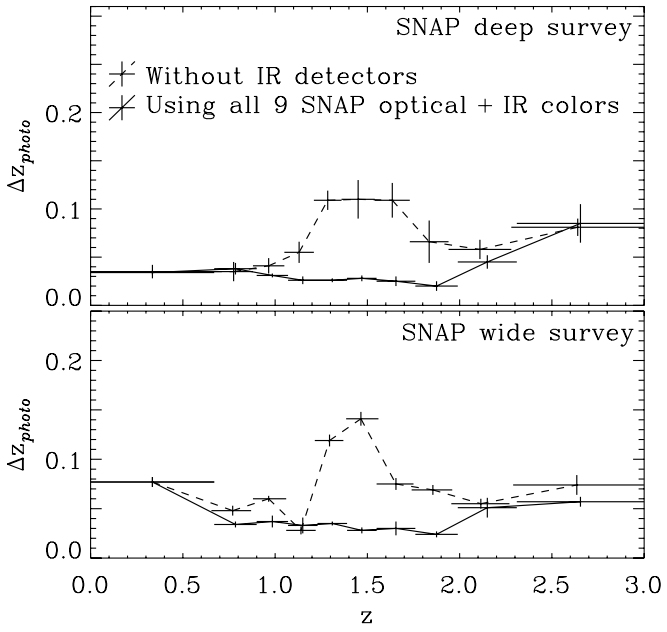

FIG. 8.—The rms scatter $\Delta z_{\rm photo}$ on photometric error estimation as a function of increasing source redshift, z. *Top*, results for the *SNAP* deep survey; *bottom*, results for the *SNAP* wide survey. In both cases, the solid line shows photometric redshift errors using observations in all nine *SNAP* optical and near-IR colors. The dashed lines show errors if the near-IR HgCdTe data are unavailable.

Figure 7 shows the precision of photometric redshifts in both the wide and deep *SNAP* surveys. All galaxy morphological types are included in this analysis. Clearly demonstrated is the need for the near-IR HgCdTe detectors, a component of the satellite where a spacecraft has a clear advantage over the ground. Figure 8 shows the accuracy of the photo-z's as a function of source (photometric) redshift. Here $\Delta z_{\rm photo}(z)$ is the rms of the core Gaussian in a double-Gaussian fit to horizontal slices through the distributions in Figure 7.

To estimate the accuracy of three-dimensional mass reconstructions (§ 5.2), we now concentrate on objects closer than $z = 1$. According to equations (6) and (7), these make up $\sim$38% of all galaxies detected in R for the wide *SNAP* survey, and $\sim$35% for the deep. For the lensing analysis (§ 3.2), we have to reject some fraction of galaxies because they were too small and not resolved. Here we assume that the same percentage of rejection applies to the $z < 1$ subsample of galaxies. This will yield a conservative estimate of the number of objects remaining in the real *SNAP* survey, because objects closer than $z = 1$ are likely to have a larger median size than the entire sample. Removing this fraction from the number density of galaxies shown in Figure 5 leaves 40 ± 5 useful galaxies per square arcminute in the *SNAP* wide survey to $z = 1$, and more than 90 arcmin^{-2} in the *SNAP* deep survey. For these galaxies only, $\Delta z_{\rm deep} = 0.034$ and $\Delta z_{\rm wide} = 0.38$ using all nine *SNAP* colors.

5. DARK MATTER MAPPING

In this section, we describe the prospects of a space-based weak-lensing survey for mapping the two- and three-dimensional distribution of dark matter. Because of the high number density of background galaxies resolved from space, this is one application where a mission like *SNAP* will fare particularly better than surveys from the ground.

5.1. *Two-dimensional Maps*

To simulate observational data, we begin with shear maps created by ray tracing through N-body simulations from Jain, Seljak, & White (2000). We then add noise to these idealized data, corresponding to the predicted levels for *SNAP* or observing conditions at the currently most successful ground-based facilities. In each case, we then attempt to recover the input projected mass distribution by inverting the map of the shear into a map of the convergence κ. Convergence is proportional to the projected mass along the line of sight, by a factor depending on the geometric distances between the observer and source and lensed galaxies (see, e.g., Bartelmann & Schneider 2001).

Figures 9 and 10 show how the projected mass can be mapped from space and from the ground. The gray scale shows the convergence κ. The top panel of Figure 9 shows a (noise-free) simulated convergence map from the ray-tracing simulations of Jain et al. (2000) for a standard CDM model. Underneath it is a version smoothed by a Gaussian kernel with an rms of $1'$ for comparison with the simulated recovery from observational data in Figure 10.

Figure 10 shows similarly smoothed mass maps that would be possible using (*top to bottom*) a ground-based survey, the *SNAP* wide survey, and the *SNAP* deep survey. These were produced by adding to κ, before smoothing, Gaussian random noise to each 1 arcmin^2 cell with an rms of $\sigma_{\bar{\gamma}}$ given by equation (5). Overlaid contours show mass concentrations detected at the 3 σ, 4 σ, and 5 σ levels. For ground-based observations we set $\sigma_\gamma = 0.39$ and used $n_g = 25$ arcmin^{-2}, as is available for ground-based surveys (e.g., Bacon et al. 2003). For the *SNAP* wide and deep surveys, the surface density of usable galaxies was taken to be $n_g = 105$ arcmin^{-2} and $n_g = 259$ arcmin^{-2}, respectively, and the rms shear noise per galaxy was taken to be $\sigma_\gamma = 0.31$ and $\sigma_\gamma = 0.36$, respectively,

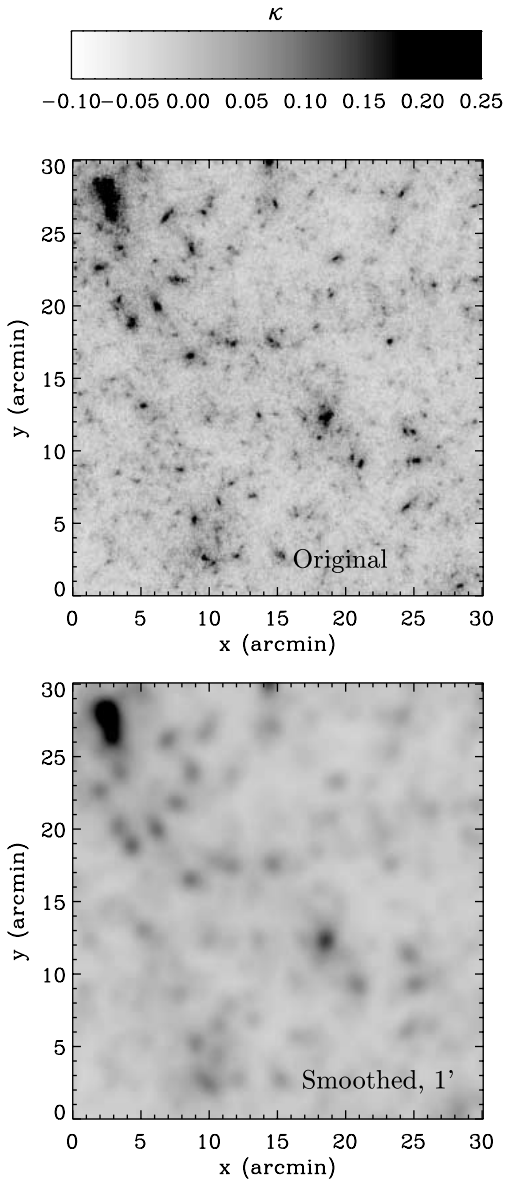

FIG. 9.—Two-dimensional convergence maps projected along a line of sight. The convergence κ is proportional to the total matter density along the line of sight and can be deduced from the shear field. *Top*: Simulated (noise-free) convergence map derived by ray-tracing through an SCDM *N*-body simulation of large-scale structure from Jain et al. (2000). The region shown is $30' \times 30'$ and the sources are assumed to lie at $z = 1$. *Bottom*: The same map, but smoothed using a Gaussian kernel with a FWHM of $1'$.

as derived from Figure 5. The galaxies are assumed to all have a redshift of $z = 1$, which is a good approximation as long as the median redshift is approximately that value. As noted above, the surface density and median redshift will actually be higher for the *SNAP* deep survey, because only exposure times corresponding to that of the HDFs were simulated.

From the ground, only for the strongest features (i.e., the most massive clusters) can a 3 σ detection be obtained. From space, the very high density of resolved background galaxies allows the recovery of uniquely detailed maps, including some of the filamentary structure and individual mass overdensities down to the scale of galaxy groups and clusters. Thus, *SNAP* offers the potential of mapping dark matter over very large fields of view, with a precision well beyond that achievable with ground-based facilities.

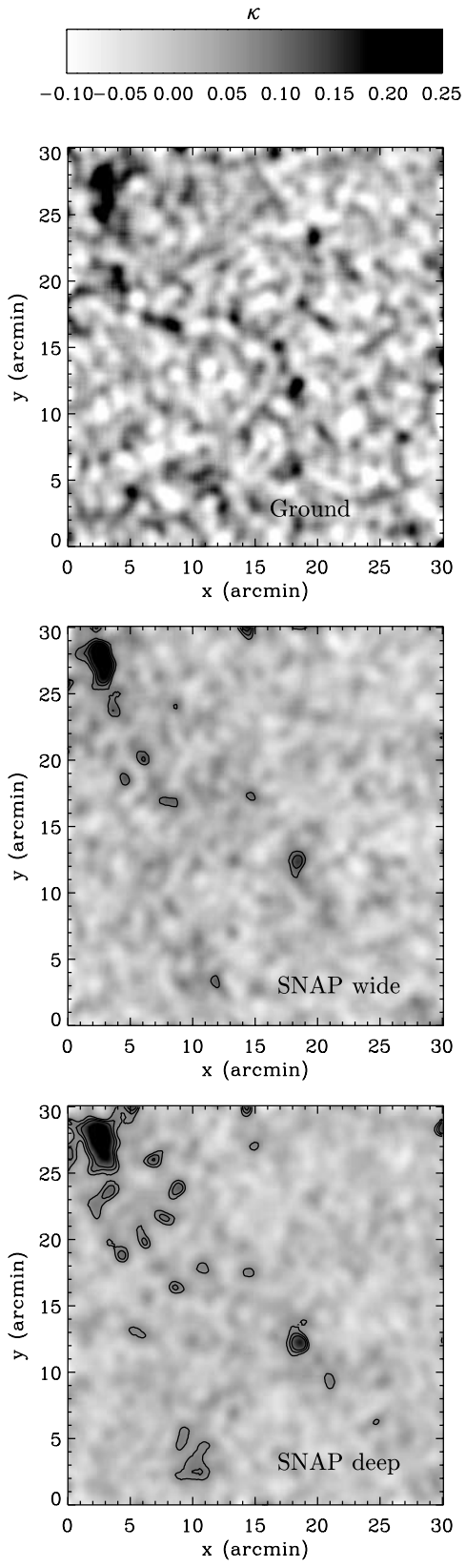

FIG. 10.—Reconstructions of the convergence map in Fig. 9 that may be feasible from weak-lensing surveys on the ground and from space. Overlaid contours show 3 σ, 4 σ, and 5 σ detection limits. *Top*, convergence κ with noise added corresponding to ground-based observations (i.e., $n_g = 25$ arcmin^{-2} and $\sigma_\gamma = 0.39$; Bacon et al. 2003); *middle*, convergence map with the expected noise properties of the wide *SNAP* survey (i.e., $n_g = 105$ arcmin^{-2} and $\sigma_\gamma = 0.31$); *bottom*, the same, but with the expected noise level of the deep *SNAP* survey (i.e., $n_g = 259$ arcmin^{-2} and $\sigma_\gamma = 0.36$).

The masses and locations of individual clusters can be extracted from such maps using, for example, the $M_{\rm ap}$ statistic (Schneider 1996; Schneider et al. 2002), which has been applied successfully to find mass peaks in several surveys (e.g., Hoekstra et al. 2002a; Erben et al. 2000) and our own work, or the inversion method of Kaiser & Squires (1993), which was used by Miyazaki et al. (2002). Marshall, Hobson, & Slosar (2003) demonstrate the effectiveness of maximum entropy techniques to identify structures in Kaiser-Squires lensing maps, using criteria set by Bayesian evidence. White, van Waerbeke, & Mackey (2002) argue that, using any detection method, a complete mass-selected cluster catalog from two-dimensional lensing data would require a high rate of false positive detections, since the prior probability is for them to be *anywhere* throughout a given survey. This has been avoided in practice by secondary cross-checks of the lensing data with spectroscopic, deep X-ray temperature, or Sunyaev-Zeldovich observations. Indeed, two previously unknown clusters have already been found in weak-lensing maps and spectroscopically confirmed by Wittman et al. (2001, 2003). However, this confusion does make it harder to resolve the debate on the possible existence of baryon-poor "dark clusters" (e.g., Dahle et al. 2003). These are a speculative population of clusters that would be physically different from, and absent from catalogs of, optically selected or X-ray–selected clusters. Remaining dark lens candidates (Erben et al. 2000; Umetsu & Futamase 2000; Miralles et al. 2002) have currently been eliminated as chance alignments of background galaxies (or possibly associations with nearby ordinary clusters; Gray et al. 2001; Erben et al. 2003). If others could be found in high-S/N weak-lensing maps, they would present a challenge to current models of structure formation and need to be accounted for in estimates of Ω_m, but they would be unique laboratories for deciphering the nature of dark matter.

5.2. *Three-dimensional Maps*

The growth of mass structures can be followed in a rudimentary way via photometric redshifts, by making two-dimensional mass maps or power spectra with source galaxies in different redshift slices (see, e.g., § 4 of Bartelmann & Schneider 2001). This technique is useful for a global statistical analysis of a survey in order to constrain cosmological parameters. It is used as such in Paper III, to predict possible constraints with *SNAP*. Tomographic measurements of shear have also led to estimates of mass and radial position of clusters (Wittman et al. 2001, 2003). After this analysis, spectroscopic redshifts were needed in order to constrain the mass further by fixing the precise radial position of clusters.

An alternative approach, in which one naturally reclaims the radial mass information as well as the transverse density, has been developed by Taylor (2001) and Hu & Keeton (2002). In this method, the shear pattern on an image is treated as a fully three-dimensional field, by including from the outset the redshift of galaxy shear estimators, as well as their two-dimensional position on the sky. Taylor (2001) shows that there is a simple inversion that relates this three-dimensional distortion field to the underlying three-dimensional gravitational potential.

Using this technique, we now demonstrate the capabilities of *SNAP* for reconstructing the three-dimensional mass distribution and locating clusters. We apply the simulations of Bacon & Taylor (2003) to the telescope and survey parameters deduced in Paper I, § 2, and § 3 and then attempt to recover the gravitational potential of two $M = 10^{14}\ M_\odot$ NFW (Navarro, Frenk, & White 1997) clusters at redshifts of 0.25 and 0.4 and separated by $0.^\circ2$ on the sky (see Figs. 4 and 5 of Bacon & Taylor 2003). Note that this is specifically a search for clusters, which induce a significant shear signal at one location rather than integrating the impact of many small objects and filamentary structures on a statistical basis over an entire shear field. Our relatively simple input model is therefore appropriate for our current purposes: it is a common occurrence that, for a line of sight with large shear, a single cluster along a line of sight is responsible for the signal.

First, we calculate the corresponding lensing potential for this field (using the prescription of Bacon & Taylor, eqs. [9]–[12]; cf. Kaiser & Squires 1993). As the lensing potential field ϕ is an integral of the shear field, we are able to reconstruct ϕ with more accuracy than the gravitational potential Φ, which is a function of the second derivative of ϕ; nevertheless, ϕ itself contains valuable three-dimensional information. This is discussed in full in Bacon & Taylor (2003). We have taken the expected number density of usable galaxies closer than $z = 1$ to be a conservative $n_g(z < 1) = 90$ arcmin^{-2}, combining results from Figure 5 and § 4. In this nearby regime we can approximate $dn/dz \propto z^2$. We have taken into account the shot noise arising from intrinsic galaxy ellipticities, using an error on shear estimators for galaxies of $\sigma_\gamma = 0.36$. We have also included an error on our photometric redshifts of $\Delta z_{\rm photo} = 0.034$ throughout $0 < z < 1$, from § 4.

Figure 11 shows the reconstruction of the lensing potential out to $z = 1$ available with the *SNAP* deep survey. The units of the lensing potential here are square radians, having chosen the differential in $\kappa = 0.5\partial^2\phi$ to be taken in units of radians. In this simulation, we see that the lower redshift cluster is very pronounced in the lensing potential, with S/N per pixel of 5.4 at $z = 1$. The lensing potential due to the higher redshift cluster is also clearly visible, with S/N per pixel of 3.0.

Figure 12 shows a reconstruction of the three-dimensional gravitational potential, using Taylor's inversion and Wiener filtering (Bacon & Taylor 2003, eqs. [8] and [40]). Even with a simulated mass of only $10^{14}\ M_\odot$, the lower redshift cluster is very pronounced, and the higher redshift cluster is also detectable at the 4.4 σ level. Extra noise peaks in Figure 12 demonstrate that the extremely low end of cluster catalogs will be subject to high false detection rates. However, this reconstruction affords measurement of masses of matter concentrations to an accuracy of $\Delta M \simeq 1.1 \times 10^{13}\ M_\odot$ at $z \simeq 0.25$ or $\Delta M \simeq 4.8 \times 10^{13}\ M_\odot$ at $z \simeq 0.5$ via χ^2 fitting (cf. Wittman et al. 2001, 2003). We can also estimate the radial position of mass concentrations from the simulated lensing data with accuracy $\Delta z \simeq 0.05$ for clusters of mass $M = 10^{14}\ M_\odot$ at $z < 0.5$ (cf. Bacon & Taylor 2003). The mass concentrations are observed at $z = 0.25$ and $z = 0.4$ as expected with peak S/Ns of 2.8 and 3.3, respectively (note that this is S/N per pixel; the overall detection significance of the cluster is as quoted above). Of course, the sensitivity of this technique drops for clusters at greater distances, as their induced lensing potential grows less within the observed redshift window (i.e., $z < 1$). In an alternative regime of interest, mass fluctuations $\delta \sim 1$ are measurable on degree scales (cf. Hu & Keeton 2002).

Equivalent simulations can be carried out for ground-based experiments, providing prospects that are more limited. The key difference that makes a space-based experiment superior over a ground-based experiment in this regard is the reduced error on shear estimates for galaxies, particularly for galaxies at $z > 0.5$, due to improved resolution and small PSF. From the

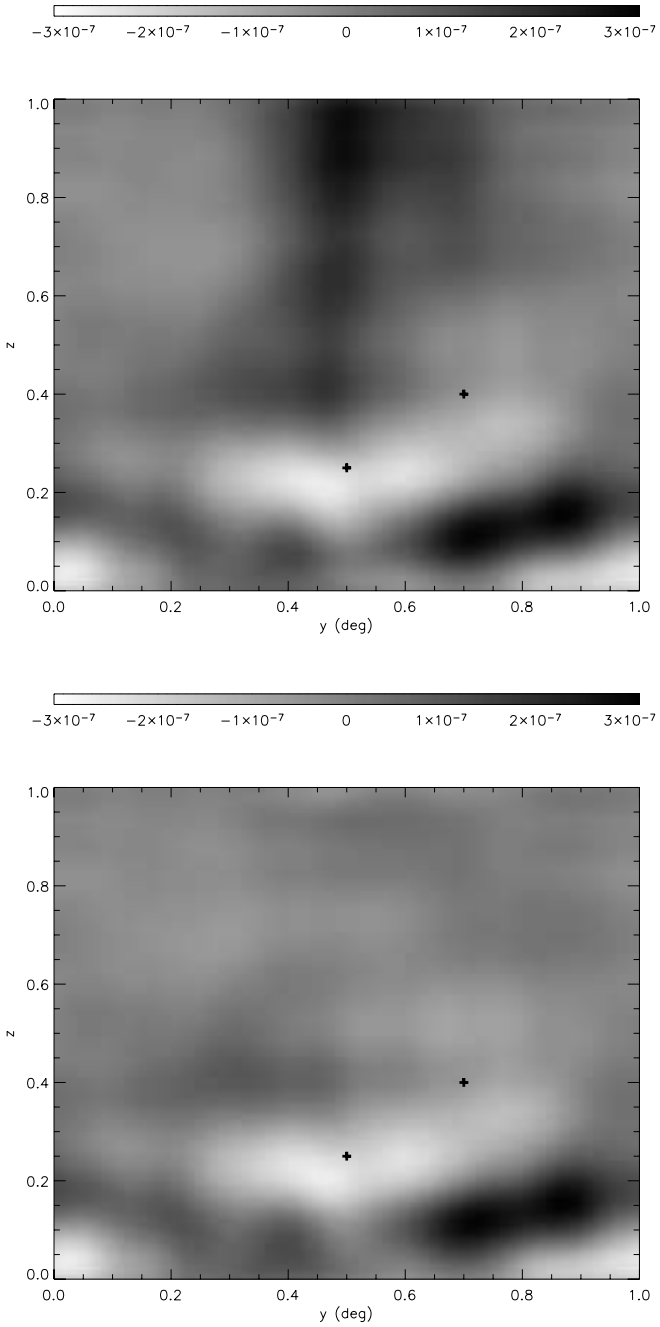

FIG. 11.—*Top*: Reconstructed lensing potential from a finite number of $z < 1$ galaxies with realistic ellipticities; $n_g = 90$ arcmin^{-2} and $\sigma_\gamma = 0.36$, as expected for the *SNAP* deep survey. The *x*-axis represents angle in degrees; the *y*-axis represents redshift. The two crosses mark the positions of the input $M = 10^{14}\ M_\odot$ NFW clusters. *Bottom*: Difference between input and recovered lensing potential fields.

ground, studies of the three-dimensional ϕ-field are restricted to measuring the mass of a cluster along the line of sight at the $\Delta M \simeq 2 \times 10^{13}\ M_\odot$ level at $z = 0.25$, with a 1.3 σ measurement of a mass of $10^{14}\ M_\odot$ at $z = 0.5$ along the line of sight of a foreground $z = 0.25$ cluster. Reconstruction of Φ in three dimensions is possible on $5'$ scales only out to a redshift of $z \simeq 0.5$ (see Bacon & Taylor 2003). Application of the full three-dimensional inversion technique to real ground-based data is currently being carried out, and even measurements of one cluster behind another cluster are possible (see review by Taylor 2003).

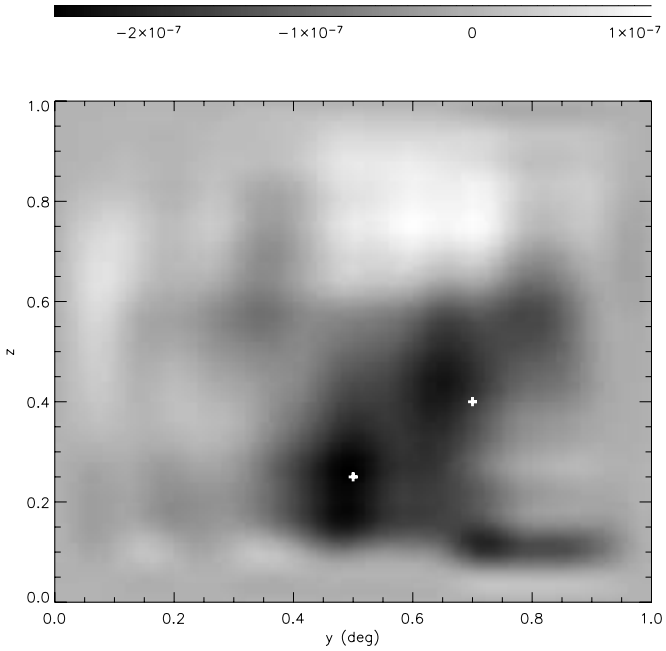

FIG. 12.—Reconstructed gravitational potential using galaxy properties of the *SNAP* deep survey, as in Fig. 11. The *x*-axis represents angle in degrees; the *y*-axis represents redshift. The two input clusters are clearly seen as the two darkest regions near the center of the image, marked with a cross.

SNAP's ability to measure the three-dimensional gravitational potential in this fashion is of great importance. One can determine the mass and density profile of several matter concentrations along a line of sight, avoiding the ambiguity of surface density lensing or projection effects and obtaining accurate measurements of the mass of matter clumps in three dimensions. One can directly compare the visible matter distribution with the underlying mass distribution to obtain important information regarding biasing and galaxy formation as a function of redshift. One can also examine the number of objects exceeding a certain mass threshold as a function of redshift (see, e.g., Viana & Liddle 1996) or reconstruct the three-dimensional power spectrum directly (see Taylor 2001) in order to obtain constraints on cosmological parameters or to test the gravitational instability paradigm that is thought to govern structure formation.

6. CONCLUSIONS

We have shown how a space-based wide-field imager like *SNAP* is ideally suited for studies of weak gravitational lensing. The aspects of this satellite's design relevant for weak lensing, and the baseline survey strategy, were presented in Paper I. A shapelet-based method for creating simulated space-based images (Massey et al. 2004; Refregier 2003a) has been used to predict *SNAP*'s sensitivity to shear, taking explicitly into account its instrumental throughput, limitations, and sensitivity.

In this paper, we have considered the baseline *SNAP* design for our predictions. As explained in Paper I, this design is almost optimal, because many requirements to find supernovae are the same as those to measure weak lensing (stable imaging, small PSF, excellent multicolor photometry).

The increased image resolution available from space makes possible the construction of high-resolution projected dark matter maps with an rms shear sensitivity of $\sim$2.5% in every

$1'$ cell for the 300 deg^2 wide *SNAP* survey and better than 1.8% for the *SNAP* deep survey (compare the expected mean signal in a ΛCDM universe of approximately 3%). Since lensing is sensitive to mass regardless of its nature and state, these maps will be unique tools for both astrophysics and cosmological parameter estimation. Statistical properties of the dark matter distribution will be precisely measured at several cosmological epochs. Constraints on Ω_m, σ_8, and w are discussed in Paper III.

SNAP's simultaneous nine-band observations also open up new opportunities for three-dimensional mapping via photometric redshift estimation (Taylor 2001; Hu & Keeton 2002; Bacon & Taylor 2003). *SNAP*'s photometry allows an excellent resolution of $\Delta z = 0.034$ in redshift. Here we have shown that *SNAP* will measure mass concentrations in a full three dimensions with a $1\,\sigma$ sensitivity of approximately $1 \times 10^{13}\,M_\odot$ at $z \simeq 0.25$ and $\simeq 5 \times 10^{13}\,M_\odot$ at $z \simeq 0.5$. In this fashion it will be possible to directly trace the nonlinear growth of mass structures, testing with high precision the gravitational instability theory.

Space-based wide-field imaging can be combined with weak gravitational lensing to produce two- and three-dimensional mass-selected cluster catalogs down to the scale of galaxy groups. Mass and light in the local universe can be mapped out with exquisite precision, thus offering exciting prospects for both astrophysics and cosmology.

We thank the Raymond and Beverly Sackler Fund for travel support. A. R. was supported in Cambridge by a PPARC Advanced Fellowship. J. R. was supported by an NRC/GSFC Research Associateship. We thank Alex Kim for his tireless efforts, and the well of information that is Mike Lampton. We are grateful for useful discussions with Douglas Clowe, Andy Fruchter, and George Smoot. Thanks also to Mike Levi and the entire *SNAP* team for collaboration and ongoing work.

REFERENCES

Aldering, G., et al. 2002, Proc. SPIE, 4835, 146
Bacon, D. J., Massey, R. J., Refregier, A. R., & Ellis, R. S. 2003, MNRAS, 344, 673
Bacon, D. J., Refregier, A., Clowe, D., & Ellis, R. S. 2001, MNRAS, 325, 1065
Bacon, D. J., & Taylor, A. N. 2003, MNRAS, 344, 1307
Bartelmann, M., & Schneider, P. 2001, Phys. Rep., 340, 291
Bernardeau, F., van Waerbeke, L., & Mellier, Y. 1997, A&A, 322, 1
Bernstein, G. M., & Jarvis, M. 2002, AJ, 123, 583
Bertin, E., & Arnouts, S. 1996, A&AS, 117, 393
Blain, A. W. 2002, ApJ, 570, L51
Bolzonella, M., Miralles, J.-M., & Pelló, R. 2000, A&A, 363, 476
Boulade, O., et al. 2000, Proc. SPIE, 4008, 657
Bridle, S. L., et al. 2004, in preparation
Brown, M. L., Taylor, A. N., Bacon, D. J., Gray, M. E., Dye, S., Meisenhemier, K., & Wolf, C. 2003, MNRAS, 341, 100
Conselice, C. J., Bershady, M. A., & Jangren, A. 2000, ApJ, 529, 886
Cooray, A., Hu, W., & Miralda-Escudé, J. 2000, ApJ, 535, L9
Dahle, H., Kaiser, N., Irgens, R. J., Lilje, P. B., & Maddox, S. J. 2002, ApJS, 139, 313
Dahle, H., Pedersen, K., Lilje, P. B., Maddox, S. J., & Kaiser, N. 2003, ApJ, 591, 662
Dalal, N., Holz, D. E., Chen, X., & Frieman, J. A. 2003, ApJ, 585, L11
Erben, T., van Waerbeke, L., Mellier, Y., Schneider, P., Cuillandre, J.-C., Castander, F. J., & Dantel-Fort, M. 2000, A&A, 355, 23
Fruchter, A. S., & Hook, R. N. 2002, PASP, 114, 144
Gray, M. E., Ellis, R. S., Lewis, J. R., McMahon, R. G., & Firth, A. E. 2001, MNRAS, 3253, 111
Gray, M. E., Taylor, A. N., Meisenheimer, K., Dye, S., Wolf, C., & Thommes, E. 2002, ApJ, 568, 141
Heavens, A., & Heymans, C. 2003, MNRAS, 339, 711
Hoekstra, H. 2003, MNRAS, 339, 1155
Hoekstra, H., van Waerbeke, L., Gladders, M. D., Mellier, Y., & Yee, H. K. C. 2002a, ApJ, 577, 604
Hoekstra, H., Yee, H. K. C., & Gladders, M. D. 2002b, ApJ, 577, 595
Hoekstra, H., Yee, H. K. C., Gladders, M. D., Barrientos, L. F., Hall, P. B., & Infante, L. 2002c, ApJ, 572, 55
Hu, W., & Keeton, C. 2002, Phys. Rev. D, 66, No. 063506
Hui, L., & Zhang, J. 2002, ApJ, submitted (astro-ph/0205512)
Huterer, D., & White, M. 2002, ApJ, 578, L95
Jain, B. 2002, ApJ, 580, L3
Jain, B., Seljak, U., & White, S. 2000, ApJ, 530, 547
Jain, B., & Taylor, A. 2003, Phys. Rev. Lett, 91, No. 141302
Jarvis, M., Bernstein, G. M., Fischer, P., Smith, D., Jain, B., Tyson, J. A., & Wittman, D. 2003, AJ, 125, 1014
Jing, Y.-P. 2002, MNRAS, 335, L89
Joffre, M., et al. 2000, ApJ, 534, L131
Kaiser, N. 2000, ApJ, 537, 555
Kaiser, N., et al. 2002, POI: The Panoramic Optical Imager (Honolulu: Inst. Astron., Univ. Hawaii)
Kaiser, N., & Squires, G. 1993, ApJ, 404, 441
Kaiser, N., Squires, G., & Broadhurst, T. 1995, ApJ, 449, 460 (KSB)
Kim, A. G., et al. 2002, Proc. SPIE, 4836, 53
King, L. J., & Schneider, P. 2003, A&A, 398, 28
Koo, D. C., et al. 1996, ApJ, 469, 535
Lampton, M. L., et al. 2002, Proc. SPIE, 4849, 215
———. 2003, Proc. SPIE, 4854, 632
Lanzetta, K. M., Yahil, A., & Fernández-Soto, A. 1996, Nature, 381, 759
Lilly, S. J., Tresse, L., Hammer, F., Crampton, D., & Le Fèvre, O. 1995, ApJ, 455, 108
Marshall, P. J., Hobson, M. P., & Slosar, A. 2003, MNRAS, 346, 489
Massey, R., Refregier, A., Conselice, C. J., & Bacon, D. J. 2004, MNRAS, 348, 214
Mellier, Y. 1999, ARA&A, 37, 127
Miralles, J.-M., et al. 2002, A&A, 388, 68
Miyazaki, S., et al. 2002, ApJ, 580, L97
Munshi, D., & Jain, B. 2001, MNRAS, 322, 107
Navarro, J. F., Frenk, C. S., & White, S. D. M. 1997, ApJ, 462, 563
Pierpaoli, E., Scott, D., & White, M. 2001, MNRAS, 325, 77
Refregier, A. 2003a, MNRAS, 338, 35
———. 2003b, ARA&A, 41, 645
Refregier, A., & Bacon, D. 2003, MNRAS, 338, 48
Refregier, A., et al. 2004, AJ, 127, 3102 (Paper III)
Refregier, A., Rhodes, J., & Groth, E. J. 2002, ApJ, 572, L131
Rhodes, J., Refregier, A., & Groth, E. J. 2000, ApJ, 536, 79 (RRG)
———. 2001, ApJ, 552, L85
Rhodes, J., et al. 2004, Astropart. Phys., 20, 377 (Paper I)
Schneider, P. 1996, MNRAS, 283, 837
Schneider, P., & Lombardi, M. 2003, A&A, 397, 809
Schneider, P., van Waerbeke, L., Kilbinger, M., & Mellier, Y. 2002, A&A, 396, 1
Smith, G. P., Edge, A. C., Eke, V. R., Nichol, R. C., Smail, I., & Kneib, J.-P. 2003, ApJ, 590, L79
Taylor, A. 2003, preprint (astro-ph/0306239)
Taylor, A. N. 2001, Phys. Rev. Lett., submitted (astro-ph/0111605)
Tyson, T. 2002, Probing Dark Matter and Dark Energy with the LSST (Washington: Natl. Acad. Sci.)
Umetsu, K., & Futamase, T. 2000, ApJ, 539, L5
van Waerbeke, L., Mellier, Y., Pelló, R., Pen, U.-L., McCracken, H. J., & Jain, B. 2002, A&A, 393, 369
van Waerbeke, L., et al. 2001, A&A, 374, 757
Viana, P. T. P., & Liddle, A. R. 1996, MNRAS, 281, 323
Viana, P. T. P., Nichol, R. C., & Liddle, A. R. 2002, ApJ, 269, L75
Weinberg, D. H., Davé, R., Katz, N., & Hernquist, L. 2004, ApJ 601, 1
Weinberg, N. N., & Kamionkowski, M. 2002, MNRAS, 337, 1269
White, M., van Waerbeke, L., & Mackey, J. 2002, ApJ, 575, 640
Williams, R., et al. 1998, BAAS, 30, 1366
Williams, R. E., et al. 1996, AJ, 112, 1335
Wittman, D., Margoniner, V. E., Tyson, J. A., Cohen, J. G., Becker, A. C., & Dell'Antonio, I. P. 2003, ApJ, 597, 218
Wittman, D., Tyson, J. A., Margoniner, V. E., Cohen, J. G., & Dell'Antonio, I. P. 2001, ApJ, 557, L89